Lab on a Chip

PAPER

View Article Online
View Journal

Cite this: DOI: 10.1039/d1lc00360g

Cascaded filter deterministic lateral displacement microchips for isolation and molecular analysis of circulating tumor cells and fusion cells†

Zongbin Liu,*[a] Yuqing Huang,[b] Wenli Liang,[c] Jing Bai,[a] Hongtao Feng,[b] Zhihao Fang,[b] Geng Tian,[c] Yanjuan Zhu,[d] Haibo Zhang,[d] Yuanxiang Wang,[e] Aixue Liu*[c] and Yan Chen *[b]

Precise isolation and analysis of circulating tumor cells (CTCs) from blood samples offer considerable potential for cancer research and personalized treatment. Currently, available CTC isolation approaches remain challenging in the quest for simple strategies to achieve cell isolation with both high separation efficiency and high purity, which limits the use of captured CTCs for downstream analyses. Here, we present a filter deterministic lateral displacement concept to achieve one-step and label-free CTC isolation with high throughput. Unlike conventional deterministic lateral displacement (DLD) devices, the proposed method uses a hydrodynamic cell sorting design by incorporating a filtration concept into a DLD structure, and enables high-throughput and clog-free isolation by a cascaded microfluidic design. The cascaded filter-DLD (CFD) design demonstrated enhanced performance for size-based cell separation, and achieved high separation efficiency (>96%), high cell purity (WBC removal rate 99.995%), high cell viability (>98%) and high processing rate (1 mL min^{-1}). Samples from lung cancer patients were analyzed using the CFD-Chip, CTCs and tumor cell–leukocyte fusion cells were efficiently collected, and changes in CTC levels were used for treatment response monitoring. The CFD-Chip platform isolated CTCs with good viability, enabling direct downstream analysis with single-cell RNA sequencing. Transcriptome analysis of enriched CTCs identified new subtypes of CTCs such as tumor cell–leukocyte fusion cells, providing insights into cancer diagnostics and therapeutics.

Received 26th May 2021,
Accepted 27th June 2021

DOI: 10.1039/d1lc00360g

rsc.li/loc

Introduction

Circulating tumor cells (CTCs) are a rare population shed from the primary tumor into the circulatory system, representing early predictors of metastasis. Compared with tissue biopsies, CTCs represent a liquid biopsy that is less invasive and carry real-time information of the tumor. Extensive studies over the most recent decade have utilized CTCs for cancer diagnosis, prognosis, treatment response monitoring, and prediction of recurrence.[1–4] However, the rarity of CTCs (1–10 cells per billion blood cells) poses a great challenge to their clinical applicability. To date, a variety of technologies have been developed to enrich and capture CTCs. These technologies can principally be divided into two categories: affinity-based[5,6] and cell size-based methods.[7–10] The affinity-based methods utilize specificity in CTC capture, but lengthy protocols may affect cell viability and prevent further downstream analysis. CellSearch is the only CTC test approved by the US Food and Drug Administration (FDA), but it still suffers from complex processes, loss of epithelial cell adhesion molecule (EpCAM) negative CTCs, and poor cell viability.[11] Conversely, size-based label-free methods offer an attractive alternative for enriching cells in an unaltered state for subsequent molecular analysis, being capable of isolating both epithelial and mesenchymal phenotypes with minimal cell loss. Microfluidics offers the potential of label-free isolation of cells based on biophysical properties, including size, stiffness, shape, and dielectric and acoustic properties.[8–10,12,13] Among these methods, passive sorting that exploits hydrodynamic phenomena and microfluidic structural design show great potential, as they can

[a] Shenzhen Zigzag Biotechnology Co., Ltd., Shenzhen, 518107, China. E-mail: zongbin.liu@zigbio.com
[b] CAS Key Laboratory of Health Informatics, Shenzhen Institutes of Advanced Technology, Chinese Academy of Sciences, Shenzhen, 518055, China. E-mail: yan.chen@siat.ac.cn
[c] Tumor Department, Shenzhen Second People's Hospital, The First Affiliated Hospital of Shenzhen University, Shenzhen, 518035, China. E-mail: liuaixue_76@sina.com
[d] Department of Oncology, Guangdong Provincial Hospital of Traditional Chinese Medicine, The Second Clinical Medical College of Guangzhou University of Chinese Medicine, Guangzhou, 510120, China
[e] Department of Cardiothoracic Surgery, Shenzhen Children's Hospital, Shenzhen, 518038, China

† Electronic supplementary information (ESI) available. See DOI: 10.1039/d1lc00360g

accomplish sorting using simple device operation with high throughput processing capabilities. Typical examples include filtration, inertial focusing, and deterministic lateral displacement (DLD).[8–10]

The deterministic lateral displacement (DLD) method was first proposed in 2004 by Huang *et al.* and has emerged as a highly promising label-free rare cell isolation technique.[14] The DLD method uses arrays of offset micropillars within a flow channel to sort cells based on diameter in a high throughput manner. A critical size for cell separation (D_c = critical diameter) is determined by the gap between the pillars and the angle of the pillar array in relation to the main direction of flow. Particles larger than D_c can be deflected by each pillar and displaced from their original lateral position at the device inlet, while particles smaller than D_c travel in a zigzag mode through the pillar array. A variety of DLD designs have been reported to separate beads, bacteria, parasites, circulating tumor cells, and blood cells.[9,15,16] Fachin *et al.* reported a state-of-the-art platform of CTC-iChip; the DLD structure was combined with inertial focusing and magnetophoresis to deplete blood cells to isolate CTCs, and achieved very high capture efficiency.[17] However, the requirement of a bulk external field generator or complex labelling may limit its practical application. To fully exploit the potential of hydrodynamics separation of DLD, it is possible to improve the DLD design to achieve higher efficiency, purity and throughput. Many improvements are introduced to increase the sorting throughput, including parallelization of several sorting arrays,[18] different pillar shapes[19,20] and arrangements.[21] Conventional DLD structures require channels close in size to the sorted cells to ensure bumping across streamlines, which thus set limitations to the design of the gaps and offset angles of the pillar array.[22]

To achieve better cell separation performance, we have proposed a hydrodynamic cell sorting design that incorporates a filtration concept into deterministic lateral displacement structures. Filtration is a simple, size-based technique that has the advantage of high throughput, but it suffers from possible blood clogging that may result in inaccurate size separation. In contrast, the DLD method can achieve accurate size separation, although the throughput is generally low. In this study, we proposed a filter-DLD structure in which filter micro-posts are arranged in the manner of DLD. The filtration structure alters the fluid field around the DLD micro-posts, allowing more precise manipulation on cell motion. As a result, the filter-DLD structure can be designed with more flexibility to achieve a higher separation throughput and small-cell depletion rate. The filter-DLD structure is further integrated into a cascaded microfluidic design consisting of blood-depletion and cell-size-separation modules. In the cascaded filter-DLD chip (CFD-Chip), the blood-depletion module was used to improve the throughput, whereas the cell-size-separation module was used to improve the capture purity.

We first employed the CFD-Chip to enrich CTCs from the blood of lung cancer patients, and demonstrated, for the first time, the potential of DLD to achieve ultra-high separation throughput with a high simultaneous depletion rate of white blood cells (WBCs). An analytical pipeline was then developed which combined marker-free isolation of circulating tumor cells and single-cell RNA sequencing to enable CTC identification at transcript levels. We anticipate that the high efficiency, label-free enrichment of CTCs using the CFD-Chip will assist in monitoring tumor dynamics in cancer patients in real-time and evaluating the response to treatment. Lung cancer is among the most threatening malignant type of tumor with the fastest-growing rates of morbidity and mortality. In the present study, more than 30 patients underwent follow-up detection of CTCs. Changes in CTC levels were correlated with clinical staging of the patients and their responses to treatments were evaluated. Furthermore, the isolated CTCs from the CFD-Chip exhibited good viability, thus providing a convenient way of combining high-throughput single-cell RNA sequencing (scRNA-seq) for downstream analysis. scRNA-seq offers the capability to identify CTCs at transcript levels, enabling the identification of new subtypes of CTCs such as tumor cell-leukocyte fusion cells as important tumor progression biomarkers. Heterogeneity analysis of mRNA expression in CTCs can further reveal novel predictive biomarkers for treatment targets, responses, and resistance.

Results and discussion

Filter deterministic lateral displacement structure

The basic working principle of filter deterministic lateral displacement (filter-DLD) is the use of filter structures to facilitate cell separation. The schematic design of the microfluidic chip that consisted of filter units is shown in Fig. 1A. The filter unit consists of two micro-posts that form a gap channel with a narrow inlet and a broad outlet, as shown in Fig. 1B. The narrow inlet was designed for a vertical fluid flow direction, with a broad outlet designed for the same direction of fluid flow. Filter units were further arranged as an offset array. When blood cells move through the filter-DLD array, small cells are partially removed by filters and partially travel in a zigzag mode in the DLD array. CTCs and large cells are retained on filters and travel in a bumping mode in the DLD array (Fig. 1C). Movie S1† clearly shows the passage of blood cells through the filter microchannel in the filter-DLD structure.

The filter-DLD structure has two unique features compared to conventional DLD structures. First, the critical separation size of the filter-DLD (D_c) is smaller than the critical size of a conventional DLD with similar array parameters. Second, the depletion rate of smaller cells in the filter-DLD array is significantly higher than that of a conventional DLD array. To better understand these effects, we performed fluid dynamics simulations on filter-DLD structures and conventional DLD structures with rectangular micro-posts.

Following the analysis by Inglis *et al.*, the fluid dynamics of the DLD structures was modelled by a 2D incompressible

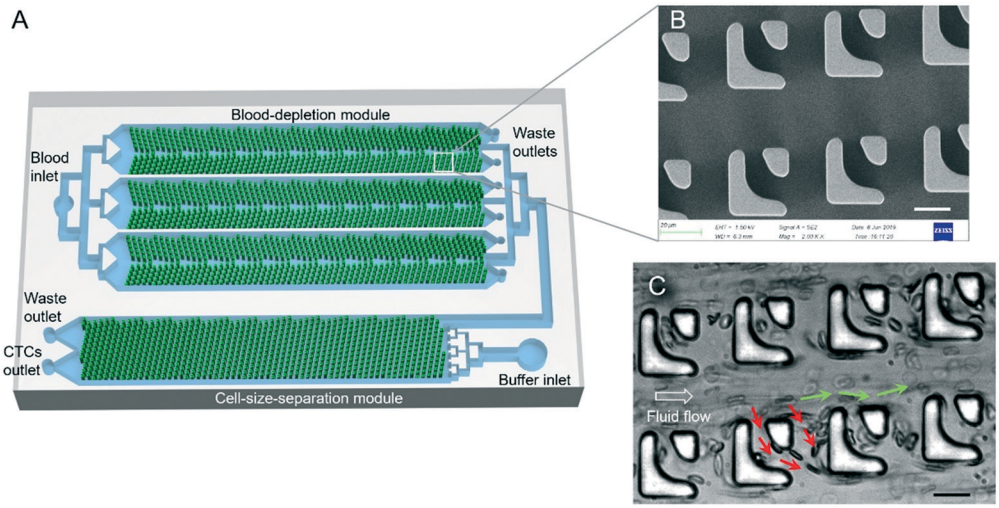

Fig. 1 Filter deterministic lateral displacement (filter-DLD) structure. (A) Schematic design of the CFD-Chip. The device is composed of a blood-depletion module, followed by a cell-size-separation module. The blood-depletion module consists of three sets of symmetric filter-DLD arrays. The cell-size-separation module consists of a filter-DLD array with gradually increasing inclination angle. (B) SEM image of the filter-DLD structure. Scale bar, 20 μm. (C) Image shows the movement of blood cells in the filter-DLD array. Red arrows indicate the trajectories of zigzag mode, green arrows indicate the trajectories of bumping mode. Scale bar, 20 μm.

Navier–Stokes equation.[23] Multiphysics finite-element solver NGSolve was used to solve the equation numerically, and the result was visualized in ParaView. The fluid streamlines are depicted in Fig. 2A and B, with red lines indicating higher speed, and blue lines indicating lower speed. The study by Huang *et al.* suggested that the total fluid flux through each gap can be divided into N flow streams,[14] and N is determined by the period of the array along the flow direction. To elucidate the separation mechanism, $N = 3$ is used as an example in our design. The width of the first stream could give us a good estimation of the critical size (D_c). Compared to the rectangular micro-post array, the higher speed regions in the filter-DLD array moved downwards, reducing the width of the first stream. Smaller cells had a higher tendency to deflect and follow the bumping mode, thus resulting in a smaller critical size.

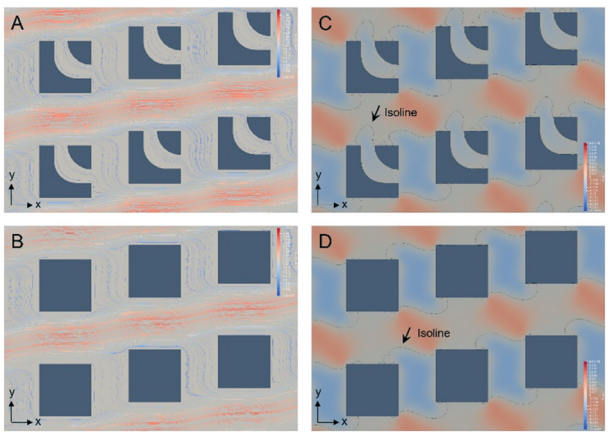

Fig. 2 Fluid dynamic simulation on DLD structures. (A and B). Fluid streamlines in the filter-DLD array and rectangular micro-post array. (C and D) Fluid velocity in the direction perpendicular to the fluid flow.

The critical size was further validated in experiments. The filter-DLD unit had a side length of 35 μm, a vertical gap width of 35 μm, a horizontal gap width of 25 μm, and an inclination angle of 9°. We used microbeads (9–18 μm) to measure the D_c of the filter-DLD chip and the rectangular micro-post DLD chip. The microbeads were perfused into the chips and collected from two outlets (Fig. S1†). The particle diameter that can distinguish the beads from the two outlets was regarded as the critical diameter. The D_c of the filter-DLD chip was estimated to be around 10 μm, while the D_c of the rectangular micro-post DLD chip was around 15 μm. To verify the critical diameter in the two DLD designs, cells with different sizes were loaded to the devices and their movements were recorded in Movie S3.† As illustrated in Fig. S2,† for the same micro-post side length, gap width and D_c, the filter-DLD structure could be designed with a larger inclination angle compared with conventional DLD structures, and this larger angle would significantly increase the width of the main channel and thus improve the separation throughput.

Fig. 2C and D show the vertical component of fluid velocity (y velocity), which is the velocity in the direction perpendicular to the fluid flow. The vertical component of the velocity provides more information about the cells' motion through barriers and their tendency to move laterally. In Fig. 2C and D, the red region indicates that the y component of velocity is positive, the blue region indicates that the y component of velocity is negative, and isoline is where the fluid velocity in the y direction is zero. From the isoline of the velocity profile, the filter-DLD induced a drag force towards the filter-DLD unit. Therefore, cells smaller than the width of the filter inlet (D_f) (*e.g.* red blood cells) had a tendency to move downwards and go through the gap channel, following a zigzag mode. As a result, the depletion

rate of smaller cells would be greatly enhanced in the filter-DLD array. This specific design ensures the removal of smaller cells at a very high flow rate, increasing the purity of isolated cell solution.

The filter-DLD structure has overcome the design limitations of a conventional DLD design, and enables precise and label-free cell sorting with higher throughput and purity. Previous studies often used increased flow rate as a strategy to improve the separation throughput. However, an increase in flow rate can adversely affect the cell viability and reduce the separation efficiency due to deformation of the cells. This is the first time to demonstrate that a filter-DLD structure can highly improve the throughput of DLD at low flow rates. Moreover, the high depletion rate of small cells (red blood cells) in the filter-DLD unit is particularly beneficial for the processing of whole blood samples. The filter-DLD structure combines the advantages of high filtration throughput with high size separation accuracy using DLD design.

Cascaded microfluidic chip design

Previous studies have reported the use of DLD structures to enrich and capture CTCs.[9,24] Long narrow microfluidic channels have generally been used in designs due to the small offset angles of DLD arrays. It is difficult to achieve high throughput separation. In the present study, filter-DLD structures were further integrated at a large scale to develop a cascaded microfluidic chip (CFD-Chip) to achieve both high throughput and high purity of CTC capture.

Fig. 3A displays a photograph of the CFD-Chip, 76 mm long and 50 mm wide. The large-area CFD-Chip consisted of more than 1 200 000 filter-DLD micro-posts. The CFD-Chip consisted of two modules, a blood-depletion module and a cell-size-separation module (Fig. 1A). In the blood-depletion module, the filter-DLD structure consisted of three sets of symmetric arrays with an offset angle of 9° and a D_c of 10 μm (Fig. 3B). Blood was perfused into the chip *via* a chip inlet. Relatively large cells, including tumor cells and a proportion of leukocytes, were finally enriched to the middle of the flow channel to be collected. In cases where only one set of DLD structures is used, flow channels are narrow and throughput cannot be improved effectively. The present study used three sets of symmetrical structures to improve the throughput by three-fold. Enriched blood from the first module and a buffer solution were perfused into the cell-size-separation module consisting of the same filter-DLD structures (Fig. 3C). The inclination angle of the filter-DLD array in the CTC separation module was gradually increased from 7° (critical size 8–8.5 μm) on the inlet side to 18° (critical size 20–22 μm) on the outlet side. In this module, a larger angle generates a larger critical separation diameter, so that cells were spatially arranged according to the size at the outlet of the separation region. The purity of CTCs collected from the CTC outlet with a relatively large size was improved.

The cascaded design of the CFD-Chip with multiple cell enrichment and purification steps in one operation not only improved the CTC capture efficiency but also reduced the use of manual labor and cost of analysis. By combining the filter-DLD concept and the cascaded chip design, we fully explored

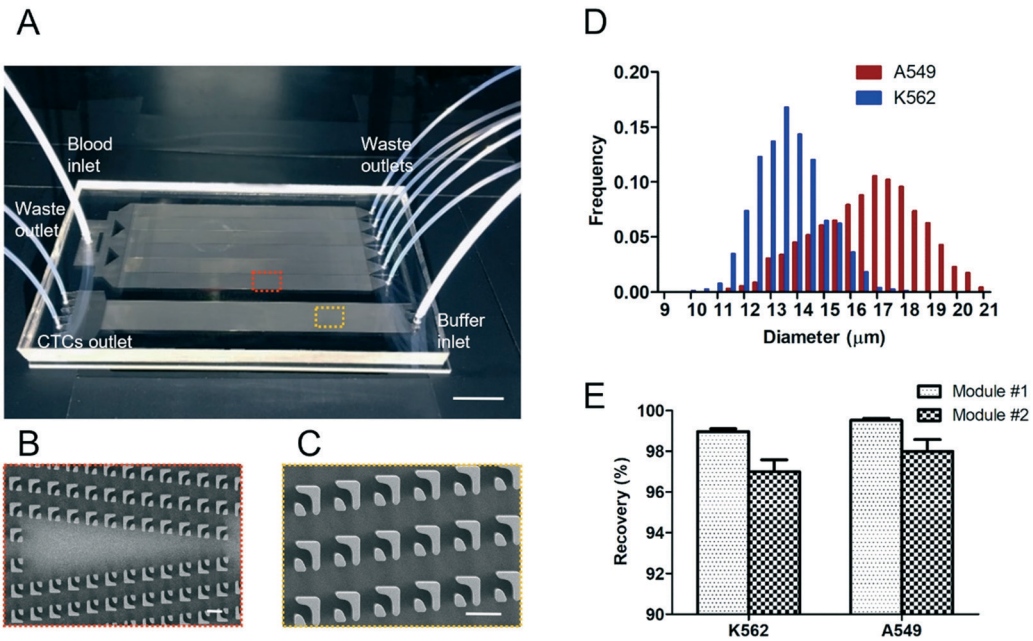

Fig. 3 Cascaded filter-DLD chip (CFD-Chip) for CTC capture. (A) Photograph of the CFD-Chip. Scale bar, 10 mm. (B) SEM image of the symmetric filer-DLD array in the blood-depletion module. Scale bar, 50 μm. (C) SEM image of the filter-DLD array in the cell-size-separation module. Scale bar, 50 μm. (D) Distribution of diameters of A549 cells and K562 cells. (E) Recovery of spiked cancer cells in the blood-depletion module (module #1) and the cell-size-separation module (module #2).

the tremendous potential of rare cell sorting based on physical properties, and developed a microfluidic platform with excellent isolation performance.

Improved CTC enrichment efficiency and capture purity

To characterize the CTC capture efficiency of the CFD-Chip, cancer cells were spiked into healthy blood samples. Two cancer cell lines, A549 and K562, were used (Fig. 3D). A549 cells are large cells with diameters between 13 μm and 20 μm that mimic large CTCs, while K562 cells are among the smallest cancer cells with diameters between 10 μm and 17 μm that mimic small CTCs.

Approximately 1000 FITC-labelled cancer cells were added to 10 mL of healthy human blood diluted 1 : 1 and perfused into the CFD-Chip at a throughput of 1 mL min^{-1}. The CTCs from the waste outlets in the first module, and the waste outlet and CTC outlet in the second module were counted. The CTC recovery of both A549 and K562 cells (Fig. 3E) was greater than 99% in the first module. In the second module, both cells achieved >96% recovery though the recovery of K562 cells was slightly smaller than that of A549 cells. The results indicate that both large and small cancer cells can be captured at high efficiency in the CFD-Chip. Coumans *et al.* reported a comparison of the recovery of large and small tumor cells using filters.[25] Although the recovery of large cells such as SK-BR-3 and MCF-7 cells was higher than 80%, the recovery of small K562 cells was less than 25%. Warkiani *et al.* reported the enrichment of different tumor cells using spiral inertial microfluidics, and achieved a high recovery of 85% for MCF-7 cells and 87% for MDA-MB-231 cells.[26] The CFD-Chip achieved higher capture efficiency than other size-based separation methods.

To evaluate the CTC capture purity, five healthy blood samples were perfused into the CFD-Chip, and white blood cells (WBCs) from the CTC outlet were counted. The number of WBCs retained from 1 mL blood ranged from 47 per mL to 232 per mL (Table S1†). The WBC count of the blood sample was 5 × 10^6 per mL in average, so the WBC removal rate was greater than 99.995%. Moreover, the red blood cell removal rate was 100%, and no pre-treatment except dilution was needed, making the whole blood processing simple and convenient.

The unique two-module cascaded separation strategy optimized the label-free cell sorting process, and achieved precise cell separation with simple operation. The high-throughput design in the first blood-depletion module removed the majority of background cells, while the second cell-size-separation module with gradually increased critical separation diameter greatly enhanced the capture purity. In the study of Coumans *et al.*, the numbers of retained WBCs were reported to be between 2000 per mL and 15 000 per mL on different filters.[25] Xiang *et al.* reported a two-stage separation method combining spiral and DLD structures, and achieved a blood cell removal ratio of 99.94%.[27] The CFD-Chip achieved much higher CTC purity than other size-based separation methods.

The CFD-Chip also provides a platform for improving the throughput of DLD at low flow rates. At a flow rate of 1 mL min^{-1}, the fluid velocity in the microfluidic channel was approximately 1.5 cm s^{-1}, much lower than the blood flow velocity (7–8 cm s^{-1}) in veins. This low flow rate induced moderate shear stress on cells, and the shear rate (~800 s^{-1}) was far less than the value (1500 s^{-1}) that might cause cell damage.[20] As a result, the isolated cells maintain good viability. The measured viability of cells from the CTC outlet was greater than 98%, sufficient for subsequent molecular analysis.

Evaluation of CTCs from lung cancer patients

CTCs from advanced non-small cell lung cancer (NSCLC) patients were captured using the CFD-Chip. Immunostaining and high throughput single-cell RNA sequencing (scRNA-Seq) were performed to identify CTCs and study their gene expression (Fig. 4E). A total of 91 blood samples from 35 stage IV NSCLC patients were analyzed. A total of 23 patients suffered from adenocarcinoma and 12 patients had squamous cell carcinoma (Table S2†).

Fig. 4A shows images of immunostained captured cells. CTCs were identified as cytokeratin (CK)+/CD45− cells with intact DAPI+ nuclei exhibiting tumor-associated morphology, such as irregular shape, deep staining, and high nuclear-cytoplasmic ratio. Although a number of cells were CK+ and CD45−, their nuclei were normal in shape, and so they were not identified as CTCs. The CTC count in 91 samples is presented in Fig. 4C. The CTC count ranged from 0 to hundreds of cells in 5 mL of blood. Tumor cell–leukocyte fusion cells were also identified by immunostaining (Fig. 4B) with CK+ and CD45+. Similar to CTCs, these fusion cells may correlate with the disease stage and predict the overall survival.[28]

Based on response evaluation criteria in solid tumors (RECIST), the disease status at the time of blood sample collection was categorized as either stable disease (SD) or progressive disease (PD). Fig. 4D displays the CTC count in samples with different disease status. When the disease status was SD, the CTC count was low, with fewer than 5 CTCs in the majority of samples. In comparison, when the disease status was PD, the CTC count in the majority of samples was greater than 5 with a mean count of greater than 60.

The CTC counts were further classified into three categories: "0", "1 ≤ CTCs < 5" and "CTCs ≥ 5" (Table S2†). In the case of SD, 23% of patients had a 0 CTC count, 45% of patients had a CTC count of 1 ≤ CTCs < 5, and 32% of patients had a CTC count of CTCs ≥ 5. In the case of PD, 89% of patients had a CTC count of CTCs ≥ 5, only 3% of patients had a 0 CTC count, and 8% of patients had a CTC count of 1 ≤ CTC < 5. The results indicate that more tumor cells disseminate into the blood circulation in patients with PD than in those with SD.

To evaluate the dynamics of CTCs, 35 patients underwent follow-up CTC detection. Fig. 5A shows the dynamics of CTC count and disease status in 9 patients

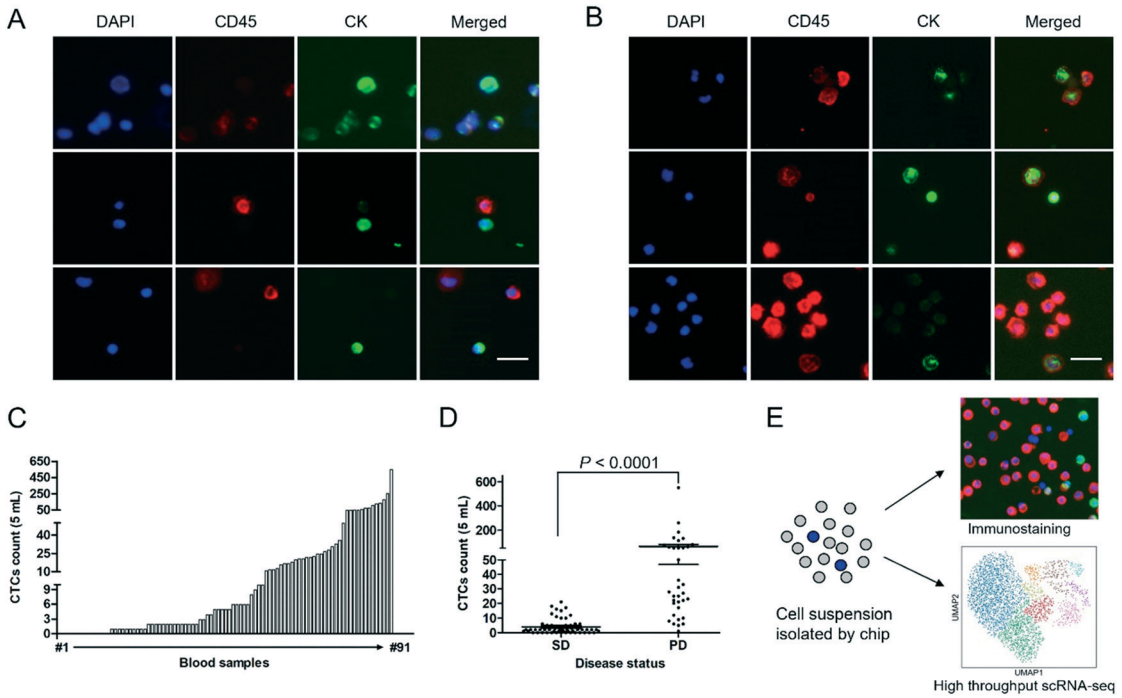

Fig. 4 Evaluation of CTCs in NSCLC patients. (A) Immunofluorescence images of CTCs. Scale bar, 50 μm. (B) Immunofluorescence images of tumor cell–leukocyte fusion cells. Scale bar, 50 μm. (C) Count of CTCs in 91 blood samples. The volume of each sample is 5 mL. (D) CTC count in patients with SD and PD. SD indicates stable disease. PD indicates progressive disease. *P* value by the non-parametric Wilcoxon–Mann–Whitney test is shown. (E) Schematic diagram of downstream molecular analysis.

where enumeration was conducted on more than three occasions. Patients #1 and #2 maintained a SD status, and their CTC count was observed at a low level. Patients #3 and #4 were initially SD but then progressed to PD, with the CTC count changing from a low to a high level. Conversely, patients #5 and #6 were initially PD then regressed back to SD. Their CTC count changed from a high to a low level. The change in disease status of patients #7, #8 and #9 was relatively complicated with repeated transitions between SD and PD. Similarly, the CTC counts repeatedly changed between low and high count. Although there was a correlation between PD with a high CTC count and SD with a low CTC count in most follow-up analyses, a number of inconsistent samples were observed. As indicated by the red arrows in the graphs of patients #4 and #9 (Fig. 5A), both CTC counts increased from 0 to more than 10, but the patients remained SD. In subsequent detection, the patient status began to change from SD to PD with a further increase in the CTC count. The results indicate that more CTCs were associated with

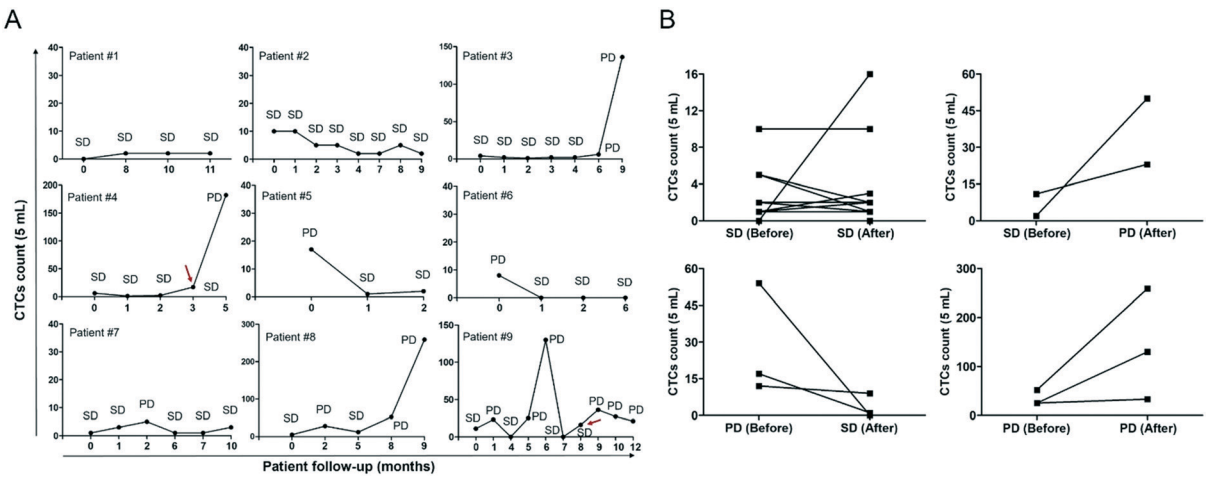

Fig. 5 (A) Dynamic monitoring of CTCs in 9 NSCLC patients. Red arrows show that the patient is SD but with an increase of CTC count. (B) Count of CTCs before and after chemotherapies. SD indicates stable disease. PD indicates progressive disease.

PD in stage IV NSCLC patients. The CTC count was an advance indicator. An increase in CTC count in SD was able to predict tumor progression.

During follow-up, a number of patients were treated with chemotherapy or targeted therapy. Changes in CTC count before and after therapy were evaluated. As shown in Fig. 5B, four changes in disease status were observed: 1) from SD to SD, 2) from SD to PD, 3) from PD to SD, and 4) from PD to PD. When patients changed from SD to SD, CTC counts were maintained at a low level with few changes, in the majority of cases. One exception was when the CTC count increased from 0 to 16. Because the CTC count is an advance indicator, the predicted change from SD to PD was observed in the subsequent analysis. The status of two patients changed from SD to PD with significant increases in CTC count, possibly due to drug resistance. Three patients with PD status changed to SD with a clear decrease in CTC count. Another three patients maintained PD status, displaying a continuous increase in CTC count, suggesting that patients did not benefit from treatment. The results in Fig. 5B suggest that the change in CTC count monitored the response to treatment of advanced NSCLC patients.

High-throughput single CTC RNA sequencing

Conventional enrichment methods based on physical properties can separate large CTCs from smaller erythrocytes and leukocytes. However, enriched cell suspensions usually still contain a significant number of background cells (10^3–10^5 per mL). The filtration-DLD method described here reduced the number of background cells from 10^5 per mL to several hundreds of cells per mL, thus allowing direct analysis of cells from enriched samples. Meanwhile, cells isolated from the CFD-Chip maintained very high viability (>98%), highly beneficial for single-cell sequencing.

We established an analytical pipeline to characterize the transcriptome profile of CTCs by combining CFD-Chip isolation and droplet-based single-cell sequencing. In this proof-of-principle study, we chose a well-established single-cell analysis protocol using 10× Genomics Chromium. Although cell loss and inefficiency are inevitable in this droplet-based method, this simple sample analysis procedure of identifying CTCs at transcript levels may provide insight into the monitoring of tumor progression.[29,30]

We obtained a blood sample from a patient with non-small-cell lung cancer (NSCLC) and used the CFD-Chip for CTC enrichment. The isolated blood sample was split into two tubes, one used for immunostaining, and another in which single-cell RNA sequencing (scRNA-seq) was conducted. Immunostaining results confirmed that there were approximately 17 CTCs in total.

In the isolated sample, a total of 3243 cells were sequenced with a median of 3226 genes per cell. Clustering analysis was performed to examine cellular heterogeneity among the isolated cells using the unsupervised learning algorithm UMAP (uniform manifold approximation and projection).[31] We then attempted to identify marker genes for each of those clusters and assigned them to known cell types. A UMAP plot of cells with predicted clusters is shown in Fig. 6A. To identify cluster-specific genes, we calculated the difference in expression of each gene between that cluster and the mean of the other clusters. Examination of cluster-specific genes with the greatest difference in expression revealed major subtypes in the isolated cells. Major groups of cells were monocytes (CD14+ mono and FCGR3A+ mono) and monocyte-derived dendritic cells. The remaining clusters were B cells, T cells, neutrophils, and megakaryocytes. The ratio of each subtype of cell was highly consistent with the size-dependent separation method since larger cells (monocytes and megakaryocytes) were enriched in the device outlet along with the CTCs. In particular, a cluster of platelet-covered cells was detected.

Due to the rarity of CTCs in blood, we developed a strategy to identify CTCs from isolated cells with gene expression profiles dramatically different from other cells. This approach identified approximately 30 CTCs. We compared the scaled expression values of candidate CTCs with the remaining cells and found numerous cancer-related genes among the top differentially expressed genes, such as PDK1, EGFL7, SOX12, FAM83D and YES1 (Fig. 6B). PDK1 is implicated in several cancer signalling pathways, such as PI3K/Akt, Ras/MAPK and Myc, and promotes tumor growth and metastasis.[32,33] Overexpression of EGFL7 has been reported in several tumors and cancer cell lines and is correlated with poor prognosis and metastasis.[34,35] It has been reported that SOX12 is a cancer stem cell marker and overexpression of SOX12 promotes proliferation and metastasis.[36,37] FAM83D is up-regulated in multiple tumors and depletion of FAM83D inhibits cell proliferation.[38] YES1 is an oncogene and drives lung cancer growth and progression.[39,40] PDK1, FAM83D, and YES1 are also promising therapeutic targets.

To analyze the molecular heterogeneity of CTCs, the expression of specific marker genes was plotted based on a UMAP clustering method. Epithelial markers such as keratin 8 (KRT8) and keratin 18 (KRT18) are commonly used markers to identify cancer cells, while CD45 (PTPRC) is a white blood cell (WBC) marker (Fig. 6C). In the CTC cluster, 10 cells were KRT+/CD45− which can be identified by immunostaining. Ten cells were KRT+/CD45+, which may be fusion cells exhibiting epithelial and leukocyte properties, and possibly represented a unique biomarker for tumor staging.[41] High-throughput scRNA-seq may identify new subtypes of CTCs, such as tumor cell–leukocyte fusion cells with KRT+/CD45+ markers.

EMT-associated genes were also expressed in cells in the CTC cluster, such as PDK1, SERPINE1, VIM, ZEB2 (transcription factor), SNAI1 (transcriptional repressor), and TGFB1 (transforming growth factor). A proportion of the CTCs displayed high mesenchymal marker expression that may exhibit a high degree of metastatic potential (Fig. 6D). In particular, we analyzed platelet marker genes, and found that

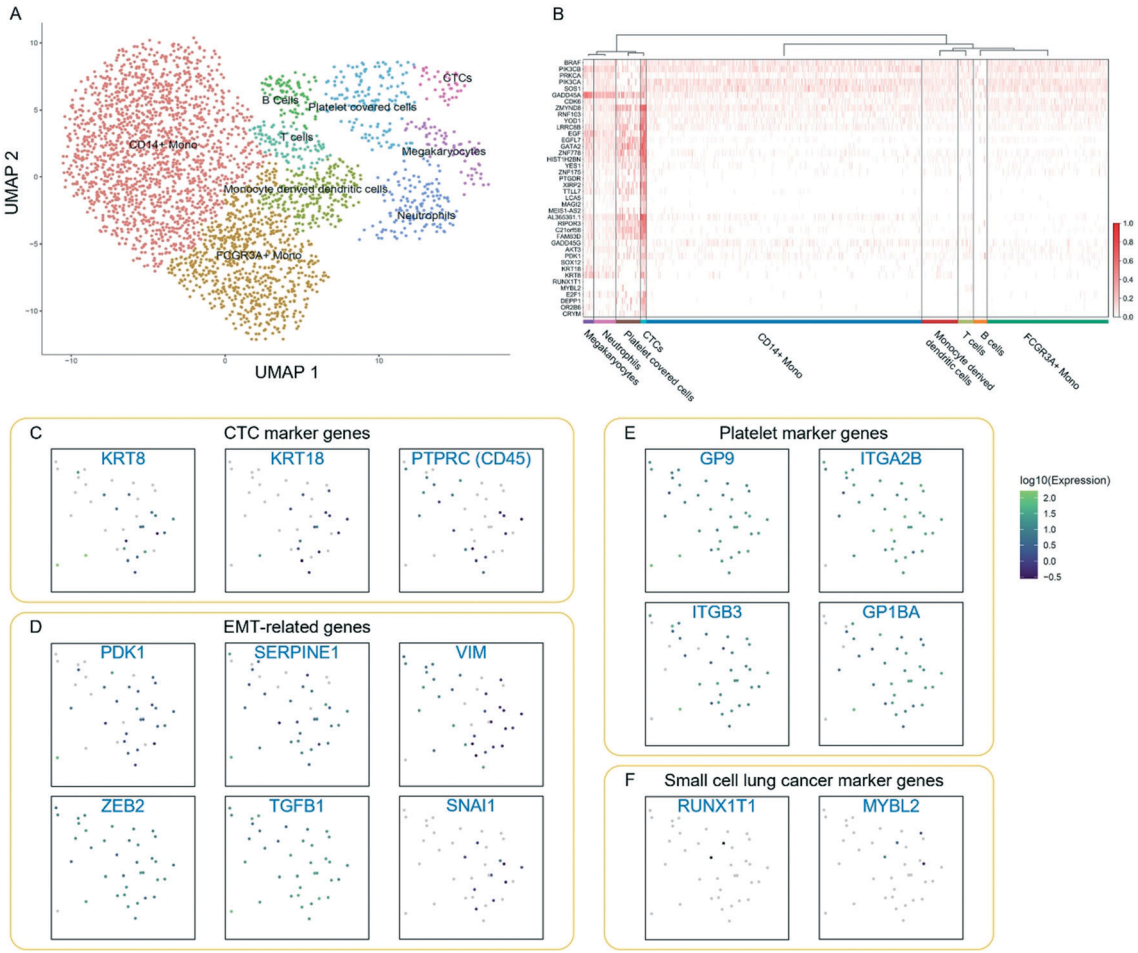

Fig. 6 Identification of CTCs using single-cell RNA sequencing. (A) A UMAP plot of the collected cells with predicted clusters based on the top-ranked marker genes. (B) Heatmap of top differentially expressed genes in the CTC cluster and other clusters. (C) UMAP plots of CTC/WBC marker genes. (D) UMAP plots of EMT-related genes. (E) UMAP plots of platelet marker genes. (F) UMAP plots of small-cell lung cancer marker genes. Blue color represents the lowest expression, and green color represents the highest expression.

these genes were overexpressed in cells in the CTC cluster (Fig. 6E). There are two possible reasons for this: 1) these CTCs may express platelet-related genes, and 2) platelets may attach to cancer cells.

The patient had been diagnosed with an adenocarcinoma subtype, however, the scRNA-seq result in Fig. 6F shows that the small-cell lung cancer (SCLC) marker RUNX1T1 was expressed in two CTCs. He *et al.* reported that RUNX1T1 was specifically amplified only in small cell lung cancer (SCLC) but not NSCLC of combined lung tumors.[42] Pro-gastrin-releasing peptide (ProGRP) is a biomarker in SCLC. The normal range of ProGRP in serum is 0–65 pg mL^{-1}. The patient had elevated levels of ProGRP (105.67 pg mL^{-1}). Compared to other CTCs, the two CTCs with the expression of RUNX1T1 also had overexpression of MYBL2 that is an important regulator of cell cycle progression, cell survival and cell differentiation. High expression of MYBL2 is correlated with poor patient outcome.[43] The results of scRNA-seq and clinical testing of ProGRP may indicate a trend of the disease transforming to SCLC. Therefore, scRNA-seq of CTCs has the potential to monitor lung cancer heterogeneity and identify NSCLC driver genes, providing a novel tool for cancer progression and metastasis research.

Experimental

Design and fabrication of CFD-Chip

The CFD-Chip was designed with blood-depletion and cell-size-separation modules (Fig. 1A) using computer-aided design (CAD) software. The CFD-Chips were fabricated using photolithography and soft lithography techniques. During photolithography, the master molds were fabricated using photoresist SU8-3050 (Microchem Corp., Naton, MA) using an EVG mask aligner (EVG 610, EV Group). Soft lithography was performed using polydimethylsiloxane (PDMS) prepolymer (Sylgard 184, Dow Corning, USA) which was mixed with a curing agent at a ratio of 10 : 1 w/w. The PDMS mixture was poured onto the master and then cured at 80 °C for 30 min. Holes for inlets and outlets were punched into the PDMS slabs. Plasma treatment was then performed to bond the PDMS slabs onto glass slides.

Evaluation of chip performance

The cancer cells A549 and K562 (ATCC, Manassas, VA) were cultured in Dulbecco's modified Eagle medium (DMEM) and Roswell Park Memorial Institute (RPMI) 1640 medium (Lonza, Walkersville, MD) supplemented with 10% fetal bovine serum (FBS) and 1% penicillin–streptomycin solution (Cellgro, MA, USA). Cell culture was maintained in a humidified incubator using 5% CO_2 at 37 °C. Cells were harvested from culture when 60% confluence by incubation with 0.0425% trypsin solution (PromoCell, Heidelberg, Germany) was achieved. A549 and K562 cells were imaged using a microscope, and their diameters were measured.

A549 and K562 cells were pre-stained using Vybrant® Dye Cycle™ Green (Life Technologies, Carlsbad, CA) then spiked into the diluted blood specimens from healthy individuals at a concentration of 100 cells per mL. Diluted blood was perfused into the CFD-Chip through the blood inlet at a flow rate of 1 mL min^{-1}. Spiked cancer cells and a number of large leukocytes were collected into the cell-size-separation module. Phosphate buffered saline (PBS) was perfused into the chip through the buffer inlet in the cell-size-separation module. The cell suspension with the most cancer cells was collected from the CTC outlet. Collected cancer cells were counted using a fluorescence microscope. Recovery of cancer cells in each module was calculated using the following equations:

$$\text{Recovery in module 1} = \frac{N_2 + N_3}{N_1} \times 100\%$$

$$\text{Recovery in module 2} = \frac{N_3}{N_1} \times 100\%$$

where N_1 is the total number of cancer cells spiked into blood, N_2 is the number of cancer cells from the waste outlet in the cell-size-separation module, and N_3 is the number of cancer cells from the CTC outlet.

Processing of patient blood samples

Blood samples from stage IV NSCLC patients were collected and processed in accordance with an IRB (Institutional Review Board) approved protocol (SIAT-IRB-190315-H0338) in Shenzhen Institutes of Advanced Technology. All patients provided informed consent to participate in this study. A 5 mL aliquot of blood was collected into an EDTA-containing tube and diluted with 4 mL PBS prior to perfusion of the blood into the CFD-Chip. The diluted blood was perfused into the CFD-Chip at a flow rate of 1 mL min^{-1}.

Immunofluorescence

Cells collected from the CTC outlet were seeded into 96-well plates coated with poly-L-lysine (Sigma-Aldrich). Paraformaldehyde (4%, Affymetrix, Santa Clara, CA) was used to fix the cells for 15 min at room temperature. Cells were washed four times using PBS then permeabilized using 0.04% TritonX-100 (Sigma-Aldrich) for 10 min at room temperature. After blocking with 3% BSA solution for 1 h, cells were incubated with a cocktail of antibodies including CD45 (1 : 100, catalog no. 555483, BD Biosciences, San Jose, CA), cytokeratin (1 : 100, ab11214, Abcam, Cambridge, MA) and Hoechst 33342 (Life Technologies, Grand Island, NY) overnight at 4 °C. After washing four times, cells were observed using a fluorescence microscope.

Single-cell RNA sequencing

Cell solutions isolated using a CFD microfluidic device were subjected to single-cell RNA sequencing (scRNA-seq) using Chromium (10× Genomics) and Illumina NGS sequencing technologies. Cell density was determined using an automated cell counter (LUNA-II). A mixture of 5 μL of 0.04% trypan blue was mixed with 5 μL of the single cell suspension to analyze cell viability. Single-cell chip loading, gel bead in emulsion (GEM) generation & barcoding, post-GEM-RT & cDNA amplification and library construction were performed in accordance with the Chromium™ Single Cell 3′ Protocol – Chemistry v2. A total of 8000 cells at a density of 1000 cells per μL were processed by 10× Genomics, with more than 3000 cells sequenced. Library construction, enzymatic fragmentation, end-repair and A-tailing were performed using the manufacturer's instructions. Generated libraries were sequenced on an Illumina HiSeq 2500 (Genergy Bio).

Sequencing data analysis

Sequencing data were analyzed using Seurat, an R package for single-cell analysis (http://satijalab.org/seurat/). Cells with more than 800 genes detected were considered successfully captured and analyzed. Cells with more than 5% mitochondrial gene expression were discarded for poor viability. Gene expression was log-normalized for principal component analysis (PCA) and uniform manifold approximation and projection (UMAP) methods. Cell clustering was performed based on the shared nearest neighbor (SNN) method. Using marker genes to define each cluster, we identified cells consistent with the profiles of monocytes, B cells, T cells, neutrophils, megakaryocytes, and monocyte-derived dendritic cells. A cluster of CTCs was also identified, with manually selected marker genes for candidate CTCs.

Statistical analysis

Data are presented as means ± s.d. A non-parametric test (Wilcoxon–Mann–Whitney test) was used to compare two groups ($P < 0.05$ was considered significant).

Conclusions

In summary, we demonstrated a novel microfluidic cascaded filter deterministic lateral displacement device to perform CTC enrichment and single-cell transcriptome analysis. The microfluidic device reported here proposed an innovative hydrodynamic structure with excellent cell separation

performance, which is difficult to accomplish using a conventional DLD design. The fully integrated microfluidic platform with cascaded filter-DLD design achieved very high sample processing throughput with simple operation, and exhibited excellent recovery of tumor cells with high efficiency and high purity. The label-free cell separation platform not only isolates CTCs, but also identifies tumor cell–leukocyte fusion cells as important tumor progression biomarkers. Moreover, the cascaded filter-DLD chip enables the molecular analysis of CTCs at single-cell resolution, providing important information for metastasis research and companion diagnostics. The novel analytical pipeline demonstrated here would provide a comprehensive understanding of the cellular heterogeneity of CTCs, and offers great promise for cancer diagnostics and therapeutics.

Author contributions

Z. L. designed the CFD-Chip. Z. L., Y. H., and J. B. performed the research. W. L., Y. Z., H. Z., G. T., and A. L. provided the blood samples. Z. L., Y. H., J. B., H. F., Z. F., Y. W., and Y. C. analyzed the data. All of the authors discussed the results. Z. L. and Y. C. prepared the manuscript.

Conflicts of interest

There are no conflicts to declare.

Acknowledgements

This work is supported by the National Natural Science Foundation of China (61875221, 61805270), Guangdong Science and Technology Department (2019A050503008), Shenzhen Fundamental Research Program (JCYJ20180507182303606, JCYJ20200109115601720), CAS Key Laboratory of Health Informatics (2011DP173015) and Youth Innovation Promotion Association of CAS (2016321). We thank Dr. Jiarui Han, Dr. Lei Zhang and Dr. Donghang Zhang for fruitful discussion in fluid dynamics simulation.

References

1 L. Carter, D. G. Rothwell, B. Mesquita, C. Smowton, H. S. Leong, F. Fernandez-Gutierrez, Y. Li, D. J. Burt, J. Antonello, C. J. Morrow, C. L. Hodgkinson, K. Morris, L. Priest, M. Carter, C. Miller, A. Hughes, F. Blackhall, C. Dive and G. Brady, *Nat. Med.*, 2017, **23**, 114–119.

2 F. Chemi, D. G. Rothwell, N. McGranahan, S. Gulati, C. Abbosh, S. P. Pearce, C. Zhou, G. A. Wilson, M. Jamal-Hanjani, N. Birkbak, J. Pierce, C. S. Kim, S. Ferdous, D. J. Burt, D. Slane-Tan, F. Gomes, D. Moore, R. Shah, M. Al Bakir, C. Hiley, S. Veeriah, Y. Summers, P. Crosbie, S. Ward, B. Mesquita, M. Dynowski, D. Biswas, J. Tugwood, F. Blackhall, C. Miller, A. Hackshaw, G. Brady, C. Swanton and C. Dive, *Nat. Med.*, 2019, **25**, 1534–1539.

3 K. Pantel and C. Alix-Panabieres, *Nat. Rev. Clin. Oncol.*, 2019, **16**, 409–424.

4 J. Sparano, A. O'Neill, K. Alpaugh, A. C. Wolff, D. W. Northfelt, C. T. Dang, G. W. Sledge and K. D. Miller, *JAMA Oncol.*, 2018, **4**, 1700–1706.

5 S. Nagrath, L. V. Sequist, S. Maheswaran, D. W. Bell, D. Irimia, L. Ulkus, M. R. Smith, E. L. Kwak, S. Digumarthy, A. Muzikansky, P. Ryan, U. J. Balis, R. G. Tompkins, D. A. Haber and M. Toner, *Nature*, 2007, **450**, 1235–1239.

6 S. Wang, K. Liu, J. Liu, Z. T. Yu, X. Xu, L. Zhao, T. Lee, E. K. Lee, J. Reiss, Y. K. Lee, L. W. Chung, J. Huang, M. Rettig, D. Seligson, K. N. Duraiswamy, C. K. Shen and H. R. Tseng, *Angew. Chem., Int. Ed.*, 2011, **50**, 3084–3088.

7 I. Cima, S. L. Kong, D. Sengupta, I. B. Tan, W. M. Phyo, D. Lee, M. Hu, C. Iliescu, I. Alexander, W. L. Goh, M. Rahmani, N. A. Suhaimi, J. H. Vo, J. A. Tai, J. H. Tan, C. Chua, R. Ten, W. J. Lim, M. H. Chew, C. A. Hauser, R. M. van Dam, W. Y. Lim, S. Prabhakar, B. Lim, P. K. Koh, P. Robson, J. Y. Ying, A. M. Hillmer and M. H. Tan, *Sci. Transl. Med.*, 2016, **8**, 345ra389.

8 H. W. Hou, M. E. Warkiani, B. L. Khoo, Z. R. Li, R. A. Soo, D. S. Tan, W. T. Lim, J. Han, A. A. Bhagat and C. T. Lim, *Sci. Rep.*, 2013, **3**, 1259.

9 Z. Liu, F. Huang, J. Du, W. Shu, H. Feng, X. Xu and Y. Chen, *Biomicrofluidics*, 2013, **7**, 11801.

10 E. Sollier, D. E. Go, J. Che, D. R. Gossett, S. O'Byrne, W. M. Weaver, N. Kummer, M. Rettig, J. Goldman, N. Nickols, S. McCloskey, R. P. Kulkarni and D. Di Carlo, *Lab Chip*, 2014, **14**, 63–77.

11 K. C. Andree, G. van Dalum and L. W. Terstappen, *Mol. Oncol.*, 2016, **10**, 395–407.

12 P. R. C. Gascoyne and S. Shim, *Cancers*, 2014, **6**, 545–579.

13 P. Li, Z. Mao, Z. Peng, L. Zhou, Y. Chen, P.-H. Huang, C. I. Truica, J. J. Drabick, W. S. El-Deiry, M. Dao, S. Suresh and T. J. Huang, *Proc. Natl. Acad. Sci. U. S. A.*, 2015, **112**, 4970.

14 L. R. Huang, E. C. Cox, R. H. Austin and J. C. Sturm, *Science*, 2004, **304**, 987–990.

15 S. H. Holm, J. P. Beech, M. P. Barrett and J. O. Tegenfeldt, *Lab Chip*, 2011, **11**, 1326–1332.

16 D. Holmes, G. Whyte, J. Bailey, N. Vergara-Irigaray, A. Ekpenyong, J. Guck and T. Duke, *Interface Focus*, 2014, **4**, 20140011.

17 F. Fachin, P. Spuhler, J. M. Martel-Foley, J. F. Edd, T. A. Barber, J. Walsh, M. Karabacak, V. Pai, M. Yu, K. Smith, H. Hwang, J. Yang, S. Shah, R. Yarmush, L. V. Sequist, S. L. Stott, S. Maheswaran, D. A. Haber, R. Kapur and M. Toner, *Sci. Rep.*, 2017, **7**, 10936.

18 J. T. Smith, B. H. Wunsch, N. Dogra, M. E. Ahsen, K. Lee, K. K. Yadav, R. Weil, M. A. Pereira, J. V. Patel, E. A. Duch, J. M. Papalia, M. F. Lofaro, M. Gupta, A. K. Tewari, C. Cordon-Cardo, G. Stolovitzky and S. M. Gifford, *Lab Chip*, 2018, **18**, 3913–3925.

19 K. K. Zeming, S. Ranjan and Y. Zhang, *Nat. Commun.*, 2013, **4**, 1625.

20 K. Loutherback, J. D'Silva, L. Liu, A. Wu, R. H. Austin and J. C. Sturm, *AIP Adv.*, 2012, **2**, 042107.

21 K. K. Zeming, T. Salafi, C. H. Chen and Y. Zhang, *Sci. Rep.*, 2016, **6**, 22934.

22 J. McGrath, M. Jimenez and H. Bridle, *Lab Chip*, 2014, **14**, 4139–4158.
23 D. W. Inglis, J. A. Davis, R. H. Austin and J. C. Sturm, *Lab Chip*, 2006, **6**, 655–658.
24 Z. Liu, W. Zhang, F. Huang, H. Feng, W. Shu, X. Xu and Y. Chen, *Biosens. Bioelectron.*, 2013, **47**, 113–119.
25 F. A. Coumans, G. van Dalum, M. Beck and L. W. Terstappen, *PLoS One*, 2013, **8**, e61770.
26 M. E. Warkiani, G. Guan, K. B. Luan, W. C. Lee, A. A. S. Bhagat, P. Kant Chaudhuri, D. S.-W. Tan, W. T. Lim, S. C. Lee, P. C. Y. Chen, C. T. Lim and J. Han, *Lab Chip*, 2014, **14**, 128–137.
27 N. Xiang, J. Wang, Q. Li, Y. Han, D. Huang and Z. Ni, *Anal. Chem.*, 2019, **91**, 10328–10334.
28 Y. Manjunath, J. B. Mitchem, K. N. Suvilesh, D. M. Avella, E. T. Kimchi, K. F. Staveley-O'Carroll, C. B. Deroche, K. Pantel, G. Li and J. T. Kaifi, *J. Thorac. Oncol.*, 2020, **15**, 1460–1471.
29 D. D'Avola, C. Villacorta-Martin, S. N. Martins-Filho, A. Craig, I. Labgaa, J. von Felden, A. Kimaada, A. Bonaccorso, P. Tabrizian, B. M. Hartmann, R. Sebra, M. Schwartz and A. Villanueva, *Sci. Rep.*, 2018, **8**, 11570.
30 D. Lambrechts, E. Wauters, B. Boeckx, S. Aibar, D. Nittner, O. Burton, A. Bassez, H. Decaluwe, A. Pircher, K. Van den Eynde, B. Weynand, E. Verbeken, P. De Leyn, A. Liston, J. Vansteenkiste, P. Carmeliet, S. Aerts and B. Thienpont, *Nat. Med.*, 2018, **24**, 1277–1289.
31 D. Sinha, A. Kumar, H. Kumar, S. Bandyopadhyay and D. Sengupta, *Nucleic Acids Res.*, 2018, **46**, e36.
32 J. Du, M. Yang, S. Chen, D. Li, Z. Chang and Z. Dong, *Oncogene*, 2016, **35**, 3314–3323.
33 P. A. Gagliardi, A. Puliafito and L. Primo, *Semin. Cancer Biol.*, 2018, **48**, 27–35.
34 G. Hong, V. Kuek, J. Shi, L. Zhou, X. Han, W. He, J. Tickner, H. Qiu, Q. Wei and J. Xu, *J. Cell. Physiol.*, 2018, **233**, 8526–8537.
35 F. Wu, L. Y. Yang, Y. F. Li, D. P. Ou, D. P. Chen and C. Fan, *Hepatology*, 2009, **50**, 1839–1850.
36 F. Du, J. Chen, H. Liu, Y. Cai, T. Cao, W. Han, X. Yi, M. Qian, D. Tian, Y. Nie, K. Wu, D. Fan and L. Xia, *Cell Death Dis.*, 2019, **10**, 239.
37 L. Wang, F. Hu, S. Shen, H. Xiao, G. Li, M. Wang and J. Mei, *Am. J. Transl. Res.*, 2017, **9**, 4003–4014.
38 D. Wang, S. Han, R. Peng, X. Wang, X. X. Yang, R. J. Yang, C. Y. Jiao, D. Ding, G. W. Ji and X. C. Li, *Biochem. Biophys. Res. Commun.*, 2015, **458**, 313–320.
39 P. D. Fan, G. Narzisi, A. D. Jayaprakash, E. Venturini, N. Robine, P. Smibert, S. Germer, H. A. Yu, E. J. Jordan, P. K. Paik, Y. Y. Janjigian, J. E. Chaft, L. Wang, A. A. Jungbluth, S. Middha, L. Spraggon, H. Qiao, C. M. Lovly, M. G. Kris, G. J. Riely, K. Politi, H. Varmus and M. Ladanyi, *Proc. Natl. Acad. Sci. U. S. A.*, 2018, **115**, E6030–E6038.
40 I. Garmendia, M. J. Pajares, F. Hermida-Prado, D. Ajona, C. Bértolo, C. Sainz, A. Lavín, A. B. Remírez, K. Valencia, H. Moreno, I. Ferrer, C. Behrens, M. Cuadrado, L. Paz-Ares, X. R. Bustelo, I. Gil-Bazo, D. Alameda, F. Lecanda, A. Calvo, E. Felip, M. Sánchez-Céspedes, I. I. Wistuba, R. Granda-Diaz, J. P. Rodrigo, J. M. García-Pedrero, R. Pio, L. M. Montuenga and J. Agorreta, *Am. J. Respir. Crit. Care Med.*, 2019, **200**, 888–899.
41 C. E. Gast, A. D. Silk, L. Zarour, L. Riegler, J. G. Burkhart, K. T. Gustafson, M. S. Parappilly, M. Roh-Johnson, J. R. Goodman, B. Olson, M. Schmidt, J. R. Swain, P. S. Davies, V. Shasthri, S. Iizuka, P. Flynn, S. Watson, J. Korkola, S. A. Courtneidge, J. M. Fischer, J. Jaboin, K. G. Billingsley, C. D. Lopez, J. Burchard, J. Gray, L. M. Coussens, B. C. Sheppard and M. H. Wong, *Sci. Adv.*, 2018, **4**, eaat7828.
42 T. He, G. Wildey, K. McColl, A. Kresak, A.-C. Tan and A. Dowlati, *J. Clin. Oncol.*, 2019, **37**, e20101.
43 J. Musa, M.-M. Aynaud, O. Mirabeau, O. Delattre and T. G. P. Grünewald, *Cell Death Dis.*, 2017, **8**, e2895.